

# A Deep Learning-based Quality Assessment and Segmentation System with a Large-scale Benchmark Dataset for Optical Coherence Tomographic Angiography Image

Yufei Wang<sup>1,2</sup>, Yiqing Shen<sup>3</sup>, Meng Yuan<sup>1</sup>, Jing Xu<sup>4</sup>, Bin Yang<sup>5</sup>, Chi Liu<sup>1,6</sup>,  
Wenjia Cai<sup>1,\*</sup>, Weijing Cheng<sup>1</sup>, Wei Wang<sup>1,\*</sup>

<sup>1</sup> State Key Laboratory of Ophthalmology,  
Zhongshan Ophthalmic Center, Sun Yat-sen University, Guangzhou 510060, China  
<sup>2</sup> Key Laboratory of Bio-Resource and Eco-Environment of Ministry of Education,  
College of Life Sciences, State Key Laboratory of Hydraulics  
and Mountain River Engineering, Sichuan University, Chengdu, Sichuan, 610064, China  
<sup>3</sup> School of Mathematical Sciences,  
Shanghai Jiao Tong University, Shanghai, 200240, China  
<sup>4</sup> Intelligent Computing Laboratory, International Graduate School,  
Tsinghua University, Shenzhen, Guangdong, 518055, China  
<sup>5</sup> Department of Ophthalmology, The Third People's  
Hospital of Zigong City, Zigong 643020, China  
<sup>6</sup> School of Computer Science, University  
Technology of Sydney, Ultimo NSW 2007, Australia

## Abstract

*Optical Coherence Tomography Angiography (OCTA) is a non-invasive and non-contacting imaging technique providing visualization of microvasculature of retina and optic nerve head in human eyes in vivo. The adequate image quality of OCTA is the prerequisite for the subsequent quantification of retinal microvasculature. Traditionally, the image quality score based on signal strength is used for discriminating low quality. However, it is insufficient for identifying artefacts such as motion and off-centration, which rely specialized knowledge and need tedious and time-consuming manual identification. One of the most primary issues in OCTA analysis is to sort out the foveal avascular zone (FAZ) region in the retina, which highly correlates with any visual acuity disease. However, the variations in OCTA visual quality affect the performance of deep learning in any downstream marginally. Moreover, filter-*

*ing the low-quality OCTA images out is both labor-intensive and time-consuming. To address these issues, we develop an automated computer-aided OCTA image processing system using deep neural networks as the classifier and segmentor to help ophthalmologists in clinical diagnosis and research. This system can be an assistive tool as it can process OCTA images of different formats to assess the quality and segment the FAZ area. The source code is freely available at <https://github.com/shanzha09/COIPS.git>.*

*Another major contribution is the large-scale OCTA dataset, namely OCTA-25K-IQA-SEG we publicize for performance evaluation. It is comprised of four subsets, namely sOCTA-3×3-10k, sOCTA-6×6-14k, sOCTA-3×3-1.1k-seg, and dOCTA-6×6-1.1k-seg, which contains a total number of 25,665 images. The large-scale OCTA dataset is available at <https://doi.org/10.5281/zenodo.5111975>, <https://doi.org/10.5281/zenodo.5111972>.*

\*Correspondance to W. Cheng and W. Wang. Y. Wang: yufei8828@gmail.com, Y. Shen: shenyq@sjtu.edu.cn, M. Yuan: dr.yuanm@qq.com, J. Xu: xu-j20@mails.tsinghua.edu.cn, B. Yang: yangbin8188@qq.com, C. Liu: chi.liu@student.uts.edu.au, W. Cai: cherylwenjia@outlook.com, W. Cheng: 18120798001@163.com, W. Wang: zoc.wangwei@yahoo.com.

## 1. Introduction

The extensive clinical application of Optical Coherence Tomography (OCT) paves the way to the visualization of

retinal microvasculature at different layers including superficial, deep, outer layer plexus, and choriocapillaris *in vivo*, rapidly and non-invasively. That is to say, OCT contributes significantly to the clinical diagnosis of retinal diseases, glaucoma, evaluation of cardiovascular, and brain health. OCT angiography (OCTA), a representative technical extension of OCT and has superior microvasculature visualization capability to that of fluorescein angiography, can generate high-resolution retinal vascular morphologic structure images by measuring the blood flow contrast in various retinal layers qualitatively and quantitatively [1]. The OCTA image of retinal vasculature has been widely utilized in disease staging and preclinical diagnosis, such as diabetic retinopathy [2]. Moreover, as a novel medical imaging technique, it plays an ever-increasing role in the optical research domain[3]. Yet, OCTA suffers from the strong image quality variation caused by many factors e.g., patient cooperation, media opacity, optical aberrations, machine-related and etc. Those artifacts of OCTA images such as defocus, shadow, motion artifact, segmentation error, loss of signal, and projection, will cause interpretation difficulty for clinicians [4]. Previous research showed that 31.6% of conventional tomographic images were ungradable [5]. 53.5% OCTA images acquired in multicenter clinical trials had severe artifacts associated with the reliability of quantitative outputs [6]. Traditionally, image quality score based on signal strength was used to include or exclude OCTA scans for further quantitative analysis. However, the commercially recommended quality index achieved only 37% to 41% sensitivity for reliable images [6]. In addition, artifacts i.e., motion, signal loss, blurriness, and off-centration could not be assessed by signal strength, however manually identification highly relies on well-trained technicians and specialized knowledge. It is a big challenge for manual assessment of OCTA artifacts in busy clinics due to the lack of human resource and insufficient time.

Another big challenge is the identification of the Foveal Avascular Zone (FAZ) in OCTA images. FAZ is a specialized region of the retina approximating the region of highest cone photoreceptor density and oxygen consumption [7, 8]. The quantitative vascular information provided by the OCTA technique is not only the extremely suited for characterizing the relationships between the morphometric properties of the FAZ and visual acuity (VA) but essential for diagnosing and follow-up the retinal vascular diseases, such as diabetic retinopathy (DR) and retinal vein occlusion (RVO). Previous bio-morphometric analysis indicated that the area of FAZ correlated with VA in DR, RVO, and age-related macular degeneration [9, 10, 11, 12, 13]. Hence, carrying out the biostatistical analysis of the relationship between FAZ area and optical diseases based on large-scale FAZ area data is on the demand. Yet, the data collection of the FAZ area still remains at the bottleneck stage: lim-

ited manual measurement. It has been reported that some OCTA systems have been embedded with automated algorithms for quantifying FAZ metrics. However, the reliability of the systems varies considerably [14, 15, 16]. On the whole, a creative and reliable technic is on the demand for the clinical diagnosis, to help physicians in unskilled but time-consuming work.

Deep learning (DL) is a promising technologies, which has received notable attention in medical imaging [17, 18, 19, 20, 21]. Currently, DL has been used for assessment of image quality in various medical imaging fields i.e., MRI, CT, ultrasound imaging, fundus photography, and OCT. For example, in the optical image field, some reliable results in OCTA image quality assessment, FAZ segmentation have been reported in previous works. Yet, the generalization ability of DL models depends marginally on the data scale. To be more specific, in OCTA image quality assessment (IQA) tasks, small datasets lead to restricted generalization ability [22, 23]. As for FAZ segmentation, the model was trained on a few high-quality FAZ images so that it cannot be used to quantify the FAZ metrics of most FAZ images [24, 25, 26]. Due to uneven OCTA image quality, automated OCTA image quality assessment and FAZ segmentation cannot be deployed to clinical diagnosis and research widely.

Considering the ophthalmologists' suffering of the exhausting manual work, we developed an automated computer-aided OCTA image processing system (COIPS) and addressed the stated challenges through the following methods. (1) We constructed a large-scale OCTA dataset considering four subsets annotated by professional ophthalmologists. This large dataset contributed to improving the generalization of the models. (2) We trained five DL-based image classification models to assess OCTA image quality automatically. Transfer learning was utilized to accelerate the training phase. (3) We trained one U-shape fully convolutional networks to segment the FAZ and quantify the FAZ metrics. (4) We combined the image format conversion, quality assessment, FAZ segmentation, FAZ metrics quantification, and reports generation into a pipeline. This pipeline is what we called COIPS.

The major contributions are summarized as follows.

1. Four large-scale OCTA image datasets annotated by professional ophthalmologists was constructed. sOCTA-3×3-10k: 10,480  $3 \times 3 \text{ mm}^2$  superficial vascular layer OCTA (sOCTA) images divided into three classes; sOCTA-6×6-14k: 14,042  $6 \times 6 \text{ mm}^2$  sOCTA images divided into three classes; sOCTA-3×3-1.1k-seg: 1,101  $3 \times 3 \text{ mm}^2$  sOCTA images with pixel-level FAZ annotation; dOCTA-6×6-1.1k-seg: 1,143  $6 \times 6 \text{ mm}^2$  deep vascular layer OCTA (dOCTA) images with pixel-level FAZ annotation. These OCTA images were labeled and annotated by professional ophthalm-

mologists. All of the images were derived from the healthy subjects or patients with diverse ophthalmic diseases i.e., DR, diabetic macular edema, cataract, age-related macular degeneration and central serous chorioretinopathy in community-based screening in Guangzhou. To our knowledge, these datasets are an order of magnitude larger than any previous public dataset in OCTA-related study.

2. An automatic COIPS based on DL was developed. According to COIPS configuration file, this system is able to transform OCTA image format, assess octa image quality, segment FAZ, quantify FAZ metrics, and generate the reports of the results automatically, which contributes to reducing the workload of ophthalmologists and saving their time.
3. Five promising quality assessment models and one FAZ segmentation models were trained on the constructed dataset. Two external testing datasets were introduced to assess the models. Our best  $3 \times 3 \text{ mm}^2$  sOCTA IQA model obtained a weighted accuracy rate of 0.91. Our best  $6 \times 6 \text{ mm}^2$  sOCTA IQA model obtained a weighted accuracy rate of 0.90. Our best  $3 \times 3 \text{ mm}^2$  sOCTA images FAZ segmentation model obtained a dice efficient of 0.95. Our best  $6 \times 6 \text{ mm}^2$  dOCTA images FAZ segmentation model obtained a dice efficient of 0.89. Detailed experimental analysis on the performance of these models was done.
4. The quality assessment and FAZ segmentation results indicate that COIPS has extracted the characteristics of OCTA images successfully. The quality assessment and FAZ segmentation achieved results of COIPS comparable to those of two experienced professional ophthalmologists.

## 2. The OCTA-25K-IQA-SEG dataset

Data-driven methods like deep learning approaches have shown their succeeding success in medical images analysis. Yet, the robustness and generalization ability of deep neural networks, either for classifier or segmenter, highly depends on the training scale. In OCTA analysis tasks, the dataset scale is very restricted to the annotation workload. We list datasets used in literary works in Table 1, describing the tasks they involved in, the available label format, public availability and etc. As it could be observed, only one small-scale OCTA dataset is made publicly available at present. Others including either the superficial vascular layer OCTA (sOCTA) or deep vascular layer OCTA (dOCTA) datasets remains property. To address this issue, one major contribution is our first attempt at constructing and publicizing a large-scale OCTA benchmark dataset, comprising of four subsets, namely sOCTA-

$3 \times 3$ -10k, sOCTA- $6 \times 6$ -14k, sOCTA- $3 \times 3$ -1.1k-seg, and dOCTA- $6 \times 6$ -1.1k-seg depending on the image size and format. Moreover, for model evaluation, our datasets provide both the image-level quality assessment annotation and the pixel-level FAZ region mask. All data used in this research have received appropriate ethic approval from Zhongshan ophthalmic center and Sichuan University. In the rest of this section, we elaborate on the construction details, including the curation of all images (c.f. Sec 2.1), our annotation strategies (c.f. Sec 2.2) and the pre-processing procedure (c.f. Sec 2.3).

### 2.1. OCTA images sources

The OCTA images used in this study were all collected from Zhongshan ophthalmic center, Sun Tat-Sen university. Specifically, a total number of 25,665 OCTA images were curated from large patient cohorts with general ophthalmic diseases i.e., DR, diabetic macular edema glaucoma, cataract, age-related macular degeneration, and central serous chorioretinopathy. All OCTA scans were digitalized with a swept-source OCTA (SS-OCTA) device (Triton DRI-OCT; Topcon Inc, Tokyo, Japan) under a 1050nm-wavelength-tunable laser at the speed of 100,000 A-scans/s. Images were scaled to  $320 \times 320$  pixels to obtain high-resolution and visualization en-face images of retinal vascular.

Depending on the image type and the field of view, we distribute whole dataset into four subsets based for study purpose. 1) sOCTA- $3 \times 3$ -10k contains a total number of 10,480  $3 \times 3 \text{ mm}^2$  superficial vascular layer OCTA (sOCTA) images. 2) sOCTA- $6 \times 6$ -14k consists of 14,042  $6 \times 6 \text{ mm}^2$  6 superficial vascular layer OCTA (sOCTA) images. 3) sOCTA- $3 \times 3$ -1.1k-seg is made up of 1,101  $3 \times 3 \text{ mm}^2$  superficial vascular layer OCTA (sOCTA) images. 4) dOCTA- $6 \times 6$ -1.1k-seg contains 1,143  $3 \times 3 \text{ mm}^2$  deep vascular layer OCTA (dOCTA) images. We did not adopt image augmentation methods in the construction of the dataset in this research to remain the original characteristic of the images.

Images in the external testing data set were curated from West China Hospital, Sichuan University for the performance evaluation.

### 2.2. Annotation strategy

Our datasets provide 2 kinds of annotation: 1) image-level classification label for quality of OCTA images, and 2) pixel-level mask for FAZ region segmentation.

The quality assessment is a classification task, where each OCTA image was labeled into one category including i) ungradable, ii) gradable, or iii) outstanding, according to the image quality, macula clarity, and retinal vascular clarity, where the detailed description is in Table 2, and some representative examples illustrated in Fig. 1. All images

Table 1. Details of the OCTA datasets used in previous works. We write ‘QA’ short for ‘quality assessment’ a image level classification task; and FAZS for ‘FAZ segmentation’ a pixel-level segmentation task; 3S short for ‘ $3 \times 3 \text{ mm}^2$  sOCTA’; 6S short for ‘ $6 \times 6 \text{ mm}^2$  sOCTA’; 3D represents ‘ $3 \times 3 \text{ mm}^2$  dOCTA’; 6D writes for ‘ $6 \times 6 \text{ mm}^2$  dOCTA’. Only one set is made publicly available, denoted by ‘ $\checkmark$ ’. We make the first attempt to publish a large-scale dataset with labels for both quality assessment and FAZ segmentation.

Dataset	Dataset scale	Field of view and image type	Major task	Label category	Public availability
[10]	21	3S	Correlation between the FAZ and visual acuity	-	$\times$
[27]	180	6S	Avascular area detection	Pixel-level	$\times$
[28]	123	6S	QA, FAZS	-	$\times$
[22]	115	6S	Classification of retinopathies	Image-level	$\times$
[23]	200	3S	QA	Image-level	$\times$
[29]	438	6S	Nonperfusion area distinguishing artifacts reduction, Pixel-level	-	$\times$
[24]	55	3S	Vessel segmentation	Pixel-level	$\checkmark$
[30]	136	3S	FAZS	Pixel-level	$\times$
[31]	180	3S	stripe noise removal	-	$\times$
[32]	406	3S, 6S	Artifacts analysis	-	$\times$
[25]	45	3D	FAZS	Pixel-level	$\times$
[26]	126	3S	FAZS	Pixel-level	$\times$
<b>sOCTA-<math>3 \times 3</math>-10k (ours)</b>	10480	3S	QA	Image-level	$\checkmark$
<b>sOCTA-<math>6 \times 6</math>-14k (ours)</b>	14042	6S	QA	Image-level	$\checkmark$
<b>sOCTA-<math>3 \times 3</math>-1.1k-seg (ours)</b>	1101	3S	FAZS	Pixel-level	$\checkmark$
<b>dOCTA-<math>6 \times 6</math>-1.1k-seg(ours)</b>	1143	3D	FAZS	Pixel-level	$\checkmark$

Table 2. Detailed descriptions for each image quality labelled category for the assessment task

Image Quality Category	Image Quality	Macular Clarity	Retinal Vascular Clarity
Ungradable	Insufficient	Macula may be off-centered or blurring	Blurring
Gradable	Moderate blurring or stripe noise	Clear	Moderate blurring
outstanding	Fully visible without blurring or with slight stripe noise	Clear	Clear or slight blurring

were labeled by three experienced ophthalmologists independently. The ambiguous images were submitted to another senior ophthalmologist to make the final judgement. In annotating pixel-level mask, Labelme (<https://github.com/wkentaro/labelme.git>), a graphical image annotation tool, was employed to contour the FAZ in OCTA image. 1,101  $3 \times 3 \text{ mm}^2$  sOCTA images chosen from gradable and outstanding OCTA images randomly in the subset sOCTA- $3 \times 3$ -10k, and 1,143  $3 \times 3 \text{ mm}^2$  dOCTA images were primiparity annotated by three experienced ophthalmologists independently. Illustrative examples for the raw images and the annotated mask can be found in Fig.2.

In order to reduce the deviation caused by subjective judgment, 10 percent of the image-level labeled and pixel-level annotated images were selected and checked by another senior experienced ophthalmologist.

### 2.3. Data preparation and separation scheme

Conclusively, a total number of 10,480  $3 \times 3 \text{ mm}^2$  sOCTA images, 14,042  $6 \times 6 \text{ mm}^2$  sOCTA images were labeled at image-level and 1,101  $3 \times 3 \text{ mm}^2$  sOCTA images, 1,143  $3 \times 3 \text{ mm}^2$  dOCTA images were further annotated with pixel-level mask. The labeled  $3 \times 3 \text{ mm}^2$ ,  $6 \times 6 \text{ mm}^2$  sOCTA images were randomly partitioned into training set, validation set, internal testing set, with hold-out method respectively. Detail descriptions of each set are shown in Table 3 and Table 4. For each patient, dOCTA

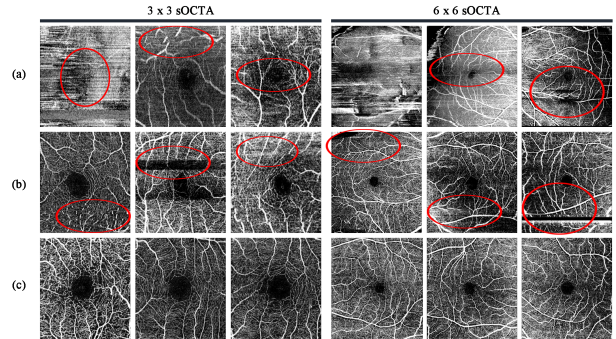


Figure 1. Illustrative OCTA examples from each quality category. (a) Ungradable; (b) Gradable; (c) outstanding. The red circle highlights the blurring region.

images and sOCTA images are taken simultaneously so that the id of both type images has same prefix. The quality assessment result of sOCTA can be applied to dOCTA.

### 2.4. Data available

We publish our dataset at <https://doi.org/10.5281/zenodo.5111975>, <https://doi.org/10.5281/zenodo.5111972>.



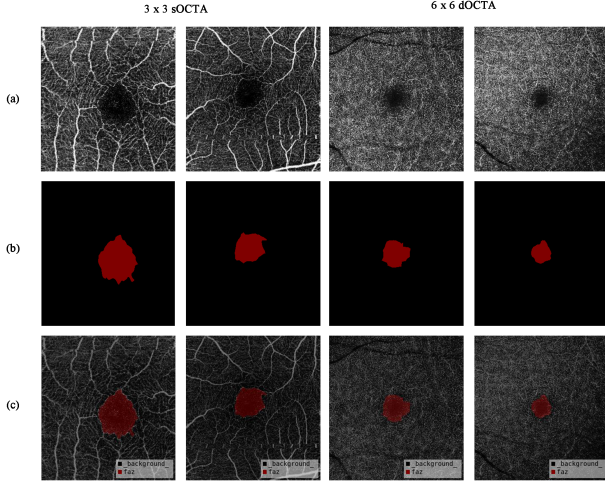


Figure 2. Examples of the OCTA images and the associated FAZ mask. (a) Original OCTA images; (b) Pixel-level ground truth for FAZ; (c) Incorporating annotations to original image.

Table 3. The scale of training, validation and testing set for quality assessment task

Sets	Quality assessment	
	sOCTA-3×3-10k	sOCTA-6×6-14k
Training	6915	9292
Testing	2965	4150
Internal testing	300	300
External testing	300	300
Total	10480	14042

Table 4. The dataset scale of training and testing set in FAZ region segmentation

Sets	FAZ segmentation	
	sOCTA-3×3-1.1k-seg	dOCTA-6×6-1.1k-seg
Training	708	800
Testing	304	343
Total	1101	1143

### 3. Methods

Quality assessment for OCTA images is a primary stage for many downstream analyses including FAZ region location. FAZ region analysis is very essential for real clinical diagnose. To address these issues, a novel automatic OCTA images analysis system is proposed for quality assessment and FAZ segmentation, namely the computer-aided OCTA image processing system (COIPS). In the section, we illustrate the overall framework of our system, and elaborate on each functional component, including a pre-processing stage, a quality assessment block, a FAZ segmentation block, FAZ metrics quantification, and the final aggregation block.

#### 3.1. Overall framework of the proposed COIPS

COIPS mainly targets to assist ophthalmologists in grading the raw OCTA images for clinical use. The major motivations are two-fold i.e., 1) quantifying FAZ metrics and 2) generating the prediction based on FAZ region measurement.

To obtain a unified format for image processing, we first covert raw OCTA images to Portable Network Graphics (PNG) images with OpenCV library (version 4.5.1.48). Afterwards, all OCTA images in png format train a quality assessment block for three-group classification i.e. ungradable, gradable, outstanding. Based on the classification results, images predicted with gradable and outstanding OCTA images will be segmented by a FAZ segmentation U-net. The ungradable images are discarded because these images do not help the disease diagnosis but only harm the computational efficiency. Lastly, the FAZ areas are computed from the segmentation masks and aggregated with a statistic model. Large-scale data of FAZ areas can be obtained through COIPS and be used to characterize the relationship between FAZ areas and optical diseases. The overall framework of the proposed COIPS is shown in Fig. 3.

We adopt image augmentation to obtain a more diverse training pattern, including random horizontal flipping and random rotation. Z-Score normalization of each image is employed to accelerate the training speed and model convergence (Patro and Sahu, 2015), as formulated by:

$$M_{ij}^{C'} = \frac{(M_{ij}^C - \bar{X})}{X_\sigma} \quad (1)$$

where  $M_{ij}^{C'}$  is the pixel-level result of Z-Score normalization,  $M_{ij}^C$  represents the pixel value of the C-th channel of the original image,  $\bar{X}$  is the mean pixel value of input image  $M_{ij}^C$ ,  $X_\sigma$  writes for the standard deviation of  $M_{ij}^C$ .

#### 3.2. Quality assessment block

In recent years, medical images classification tasks have benefited greatly from domain adaption including transfer learning, since the restricted quantity of data in the medical domain. For example, to detect and classify the malignant cells in breast cytology images, Khan et al. proposed a CNN-based model which was pre-trained on ImageNet. Then, the model was trained on 6,000 breast cancer histopathology images and achieved an accuracy of 97.525% on 2,000 breast cancer histopathology images [33]. Swati et al. employed transfer learning and they fine-tuned VGG19 to classify the brain tumor for MRI images. Their methods achieved an average accuracy of 94.82% under five-fold cross-validation with block-wise fine-tuning [34]. With the use of fine-tuning on pre-trained models, researchers can accelerate the convergence speed as well as achieve higher generalization ability [35]. Quality assess-

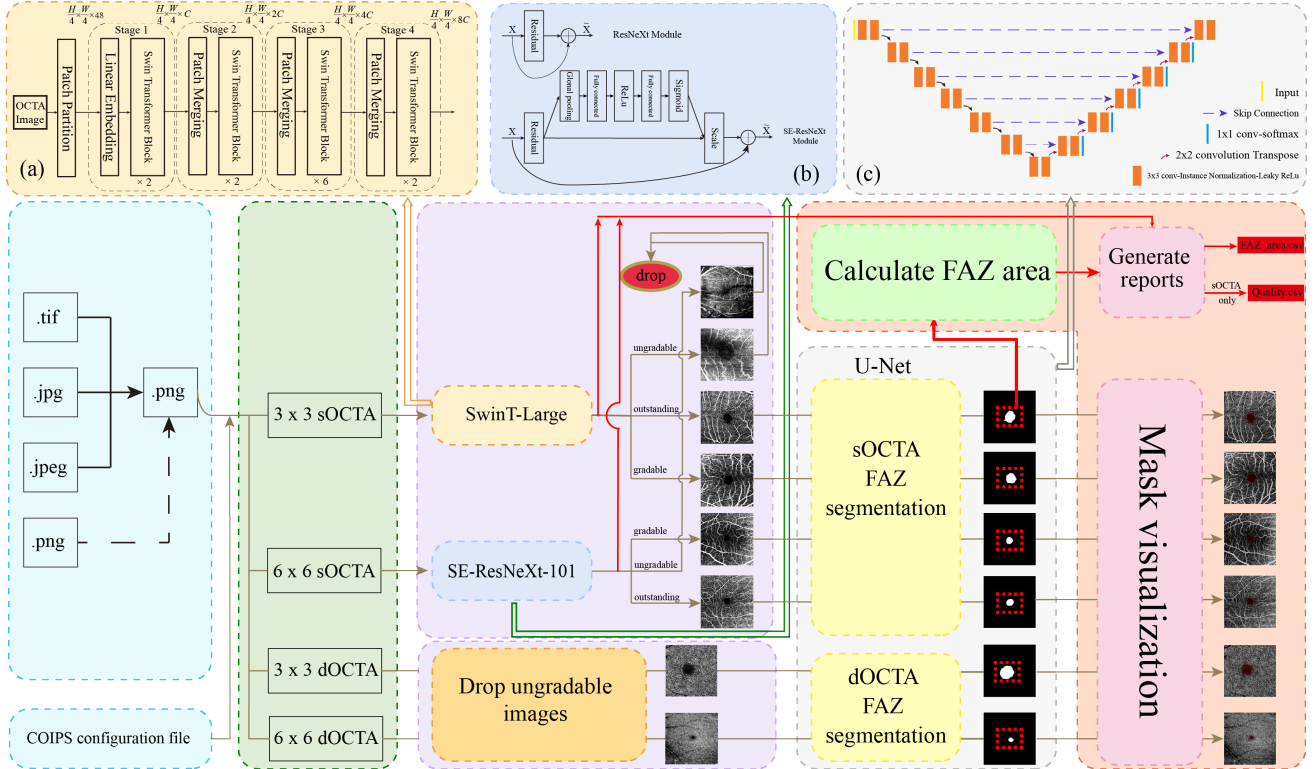


Figure 3. Overview of our COIPS. This system can assign an appropriate pipeline based on the input configuration file; (a) The architecture of Swin Transformer (SwinT); (b) Schema of SE-ResNeXt-101 modules; (c) Network architectures generated for FAZ segmentation. OCTA images are first assessed for their visual quality. Based on the classification result of sOCTA images, the ungradable dOCTA images are discarded, while other images are further segmented for FAZ location. In the next stage, the diagnostic suggestion is derived from an aggregation model based on the segmentation result.

ment of OCTA images can help ophthalmologists to eliminate the unhelpful artifacts OCTA images. Hence, we also adopt the pre-trained networks as the backbone for three-class classification tasks in quality assessment.

The proposed COIPS is CNN-architecture-independent. In this study, five state-of-the-art pre-trained models were adopted as a case study for their outstanding performance on natural image classification and compact architecture. Specifically, we use ResNet-101 [36], Inception-V3 [37], Efficientnet-B7 [38], SE-ResNeXt-101 [39, 40], and Swin-Transformer [41] as the backbone feature extractor for assessing the OCTA quality. We fine-tuned the last fully connected layer to fit our dataset, while the parameters in the top layers are frozen. It was a common case that the numbers of data instances from each category were not balanced (shown in Fig. 4), hence a modified cross-entropy loss function [42] is employed to train our network. It assigns weights to the different categories to focus the target network on the categories with fewer samples i.e.,

$$weight_i = \frac{\sum_{i=1}^N X_i}{N X_i} \quad (2)$$

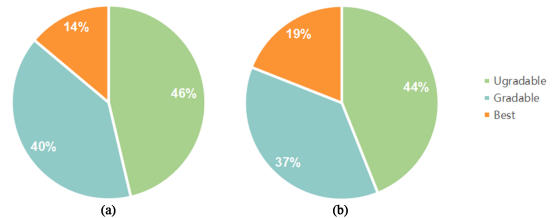


Figure 4. Category proportion in two datasets. (a) sOCTA-3×3-10k; (b) sOCTA-6×6-14k.

$$Y_i = \begin{cases} 0, & x_i \neq y_i \\ 1, & x_i = y_i \end{cases} \quad (3)$$

$$loss(x_i, y_i) = -weight_i \sum Y_i \log(P_i) \quad (4)$$

$$loss = \frac{\sum_{i=1}^N loss(x_i, y_i)}{\sum_{i=1}^N weight_i} \quad (5)$$

where  $X_i$  is the total number of class  $i$ ,  $N$  is the number of category,  $x_i$  is the predicted label of class  $i$ ,  $y_i$  is the ground truth of class  $i$ ,  $P_i$  is the probability of  $y_i$ .

All the images were resized to  $224 \times 224$  as the input to ResNet-101, Inception-V3, Efficientnet-B7, SE-ResNeXt-101,  $384 \times 384$  for Swin-Transformer, and  $600 \times 600$  for Efficient-B7. The images were horizontally flipped with a probability of 0.5 and rotated with the angle varied between -15 degrees to 15 degrees randomly for augment.

Prior to the FAZ segmentation in the next section, it is essential to exclude the ungradable images in the quality assessment block. Since these images do not contribute to disease diagnosis and the macular center of them are blurry or even none, but only bring extra computational cost.

### 3.3. FAZ segmentation and visualization

U-Net, an encoder-decoder network architecture, is a primary DL choice for increasing segmentation and quantification tasks and has been the basis of many DL models in biomedical image analysis [43, 44, 45]. Falk et al. developed an ImageJ plugin based on U-net for cell counting and achieved detection and morphometry with the average intersection over union (IoU) of 85% [44]. Guo et al. proposed a customized encoder-decoder network for deep FAZ segmentation with a boundary alignment module and boundary supervision modules and obtained an average Dice of 0.88 [25]. Isensee et al. reported results on 53 segmentation tasks on 23 public datasets used in international biomedical segmentation competitions and generated 39 state-of-the-art (sota) segmentation models. These tasks cover a large proportion of the dataset variability in the medical domain [46]. They also launched a framework, namely nnU-Net. This framework can configure itself automatically with configuration derived by distilling expert knowledge learned from the 53 medical segmentation tasks, which achieved a higher generalization ability than that of models configured on a single dataset. Previous theoretical and empirical results suggest that sophisticated architectural variations are not necessary to obtain a sota model in medical images processing [47, 48, 49].

Accurate FAZ segmentation for OCTA images is the prerequisite for precise quantification of FAZ areas [25]. Due to various artifacts, conventional medical image analysis techniques such as the denoising filters were not effective enough to the unclear boundary of FAZ, while manual measurement of the FAZ area is unskilled but time-consuming work. In this study, we constructed a U-Net alike architecture based on nnU-Net framework (<https://github.com/MIC-DKFZ/nnUNet.git>), as shown in Fig. 3 (c). We fine-tuned the architecture to fit our OCTA datasets in segmenting the FAZ region. The network configurations are shown in Table 5. Dice loss defined in Eq. (7) originally targets to maximize the  $F_1$  Score. The dice

loss function is well suited to address the class imbalance, but it will cause unstable training. To achieve better training stability and higher segmentation accuracy, a cross-entropy loss function defined in Eq. (8) was incorporated with dice loss to train the model.

$$\begin{aligned} DiceCoefficient &= \frac{2|SR \cap GT| + 1}{|SR| + |GT| + 1} \\ &= \frac{2TP + 1}{2TP + FN + FP + 1} \end{aligned} \quad (6)$$

$$Loss_{dice} = 1 - DiceCoefficient = F_1score \quad (7)$$

where  $SR$  is the segmentation result,  $GT$  is the ground truth.  $TP$  denotes true positives (correctly predicted FAZ pixels),  $FP$  denotes false positives (incorrectly predicted FAZ pixels), and  $FN$  denotes false negatives (incorrectly rejected FAZ pixels), similarly hereinafter.

$$Loss_{ce} = - \sum R_i \log(S_i) \quad (8)$$

where  $R_i$  donates the label of pixel  $i$ ,  $S_i$  donates the prediction of pixel  $i$ .

To be more specific, the total loss function is formulated as the linear combination of CE-loss and Dice-loss:

$$Loss_{Total} = \lambda \times Loss_{CE} + (1 - \lambda) \times Loss_{dice} \quad (9)$$

where  $weight_{ce}$  and  $weight_{dice}$  are the weight to balance two parts of loss  $Loss_{CE}$  and  $Loss_{dice}$ . In this study,  $\lambda = 0.5$ .

To obtain an operating system independent, we reconstructed the nnU-Net framework to run inference on Linux, Windows, and macOS, as provided in the GitHub link. The inferred masks were visualized with SimpleITK library (version 2.0.2) and Pillow library (version 8.1.2).

### 3.4. FAZ metric quantification

In the this stage, the reports of quality assessment and FAZ metrics were generated for diagnosis. The area of FAZ is calculated as:

$$S_{FAZ} = \frac{N_{mask}a^2}{z^2} \quad (10)$$

where  $N_{mask}$  is the pixel number of predicted FAZ mask,  $a$  is the true length at retina that the OCTA image shows,  $z$  is the horizontal pixel value of FAZ mask image.

## 4. Experiment and results

In this section, we describe our experimental settings and the empirical results.

### 4.1. Platform

We utilized PyTorch (<https://pytorch.org>, version 1.8.1) with Python environment (version 3.9.2) to implement all experiments. All of the trials were carried out using an Ubuntu workstation with an i7-7700k CPU and an NVIDIA GEFORCE RTX 3090 GPU, 64 GB of RAM.

### 4.2. Experimental setting-up

**Quality assessment:** All the weights of models used in this study were pretrained on the ImageNet dataset [50]. All of the training run for a fixed length of 300 epochs. To save computing resources and time, the program was early stopped when the test loss was no longer reduced within 20 epochs. We also warmed up the training with the learning rate of 0.0000005 for 20 epochs when trained Swin-Transformer-Large model. As for optimizer, Adam with an initial learning rate of 0.001 was used for training ResNet101, Inception-V3, SE-ResNeXt101, and Efficinet-B7 [51]. AdamW with an initial learning rate of 0.0005 was used for training Swin-Transformer-Large [52]. The learning rate was reduced during training using ‘‘CosineAnnealingLR’’ schedule with ‘‘T\_MAX’’ of 5 [53].

**FAZ segmentation:** Stochastic gradient descent (SGD) was chosen as the optimizer with an initial learning rate of 0.01 and Nesterov momentum of 0.99 [54]. 5-fold-cross-validation was trained and the best one was used to infer. We employed the ‘‘poly’’ learning rate (polyLR) policy as a learning rate reducing schedule with the exponent of 0.9 [55]. All of the other configuration parameters were generated by the nnU-Net framework, automatically.

### 4.3. Evaluation metrics

**Quality assessment:** We adopted a variety of measures commonly used for classification tasks to assess the performance of the quality assessment models, including accuracy (Acc), precision (Pre), area under the receiver operating characteristic curve (AUC),  $F_1$  score, and confusion matrix. The model with the highest validation accuracy was selected as the backbone classifier for FAZ segmentation evaluation.

**FAZ segmentation:** We employ the following metrics: dice coefficient, Jaccard index, precision and recall. Jaccard index, precision and recall are defined as:

$$J_{index} = \frac{|GT \cap SR|}{|GT \cup SR|} \tag{11}$$

$$precision = \frac{TP}{TP + FP} \tag{12}$$

$$recall = \frac{TP}{TP + FN} \tag{13}$$

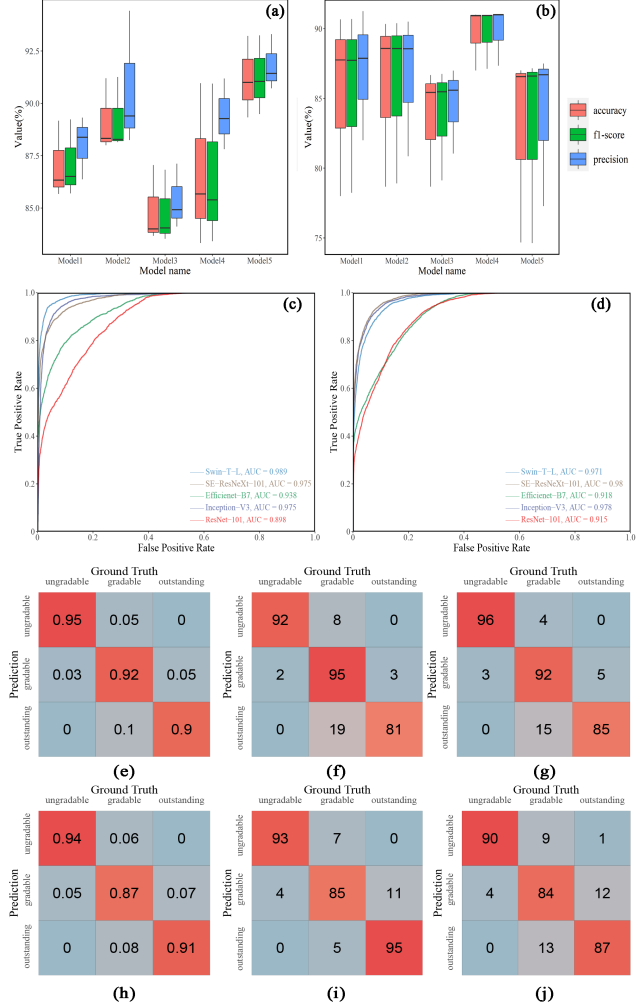


Figure 5. Results visualization of all of the models. (a) – (b) Box-plot of accuracy, precision and  $F_1$  score of different models for  $3 \times 3 \text{ mm}^2$  sOCTA (left) and  $6 \times 6 \text{ mm}^2$  sOCTA (right) quality assessment; (c) – (d) ROC curve of different models for  $3 \times 3 \text{ mm}^2$  sOCTA (left) and  $6 \times 6 \text{ mm}^2$  sOCTA (right) quality assessment; (e) – (g) Confusion Matrix plot of predictions of testing set (left), internal testing set (middle) and external testing set (right) using Swin-transformer-Large to assess  $3 \times 3 \text{ mm}^2$  sOCTA images; (h) – (j) Confusion Matrix plot of predictions of testing set (left), internal testing set (middle) and external testing set (right) using SE-ResNeXt-101 to assess  $6 \times 6 \text{ mm}^2$  sOCTA images. Where ‘Model1’ is short for ‘Efficinet-B7’, ‘Model2’ is short for ‘Inception-V3’, ‘Model3’ is short for ‘ResNet-101’, ‘Model4’ is short for ‘SE-ResNeXt-101’, ‘Model5’ is short for ‘Swin-Transformer-Large’.

### 4.4. Results and visualization

**Quality assessment:** Table 6 demonstrates the classification performance of quality assessment models. More detailed evaluations including Acc, Pre, and  $F_1$  score on each sub-dataset are shown in Supplementary Note, Table



Table 5. Network configurations for U-Net

Configuration	Assigned Parameter
Batch size	64
Patch size	[512, 512]
Number of pooling per axis	[7, 7]
Down-sampling strides	[[2, 2], [2, 2], [2, 2], [2, 2], [2, 2], [2, 2], [2, 2]]
Convolution kernel sizes	[[3, 3], [3, 3], [3, 3], [3, 3], [3, 3], [3, 3], [3, 3], [3, 3], [3, 3]]

S1 – S10. The box-plot figures in Fig. 5, (a) – (b) suggests that Swin-Transformer-Large outperforms other classification models on  $3 \times 3 \text{ mm}^2$  sOCTA quality assessment; and SE-ResNeXt-101 stands out on  $6 \times 6 \text{ mm}^2$  sOCTA quality assessment in this study. Specifically, Swin-Transformer-Large achieves an accuracy of 0.91, a precision of 0.92, and an  $F_1$  score of 0.91 on  $3 \times 3 \text{ mm}^2$  sOCTA testing data set, marginally succeeds the other four network architectures. SE-ResNeXt-101 achieve an overall accuracy of 0.90, a precision of 0.90 and a  $F_1$  score of 0.90 on  $6 \times 6 \text{ mm}^2$  sOCTA testing data set. The Receiver Operating Characteristic (ROC) curve evaluates the sensitivity of the classification models, are illustrated in Fig. 5, (c) – (d). The ROC curve figures of each category are shown in Supplementary Note, Fig. S1 – S10. It is observable that Swin-Transformer-Large and SE-ResNeXt-101 performs better than other models in terms of  $3 \times 3 \text{ mm}^2$ ,  $6 \times 6 \text{ mm}^2$  sOCTA quality assessment, respectively. Both of Swin-Transformer-Large and SE-ResNeXt-101 can achieve an Auc of 0.98. The confusion matrix shows a precise number of predictions for each dataset in Fig. 5, (e) – (j). It can be seen that there are no significant differences in prediction performance among the three categories. Therefore, we used Swin-Transformer-Large and SE-ResNeXt-101 to assess the quality of  $3 \times 3 \text{ mm}^2$ ,  $6 \times 6 \text{ mm}^2$  sOCTA images, respectively for the downstream FAZ segmentation task.

**FAZ segmentation:** The overall performance of the FAZ segmentation model on two datasets is shown in Table 7. The model trained on sOCTA- $3 \times 3$ -1.1k-seg achieves a dice coefficient of 0.95, a Jaccard index of 0.91, a precision of 0.96, and a recall of 0.95. Trained on dOCTA- $6 \times 6$ -1.1k-seg dataset, the model achieved a dice coefficient of 0.89, a Jaccard index of 0.79, a precision of 0.89, and a recall of 0.89. We visualized the FAZ segmentation mask on two subsets compared with ground truth in Fig. 6 and Fig. 7. As shown in the figures, the model can locate the FAZ area accurately with a smooth boundary.

## 5. Conclusion and Discussion

In recent years, the OCTA technique shows promising results in getting the images of the smallest capillaries from the retina without the necessity of a contrast agent [24]. However, the pathologic information OCTA images reflect highly depends on the quality of the image. To address this

issue, we construct an effective image-level quality assessment neural network classifier. Besides, FAZ segmentation of OCTA images shows great significance to clinical diagnosis as well as for academic research propose.

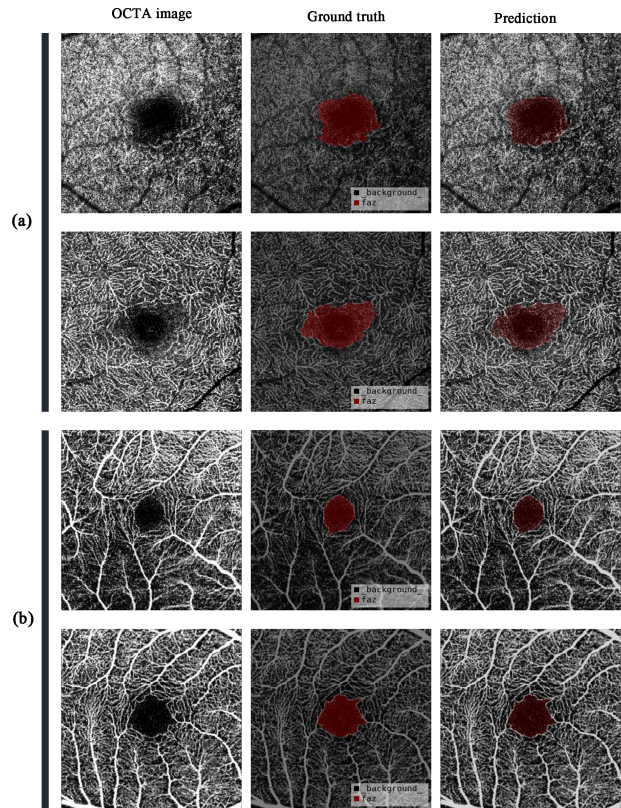


Figure 6. Segmentation results of  $3 \times 3 \text{ mm}^2$  OCTA images against the ground truth. (a) Prediction of dOCTA images; (b) Prediction of sOCTA images.

While the existing solutions for FAZ quantification including built-in programs, conventional images processing techniques, and manual measurement, are labor-intensive and computationally costly. Furthermore, limited by methods of FAZ area measurement, there is little research on the correlation between FAZ area and retinal vascular diseases. Therefore, we propose a novel automated COIPS in this research to address all these issues. This system can serve as assistive tools to ophthalmologists by reducing their many workloads. Our system also shows large gener-

Table 6. Overall performance of quality assessment models. The number in the Table is the average of testing set, internal testing set and external testing set, respectively. where  $3 \times 3$  is short for ' $3 \times 3 \text{ mm}^2$  sOCTA';  $6 \times 6$  is short for ' $6 \times 6 \text{ mm}^2$  sOCTA'.

Metrics	ResNet-101		SE-ResNeXt-101		Efficientnet-B7		Swin-T-Large		Inception-V3	
	$3 \times 3$	$6 \times 6$	$3 \times 3$	$6 \times 6$	$3 \times 3$	$6 \times 6$	$3 \times 3$	$6 \times 6$	$3 \times 3$	$6 \times 6$
Acc	0.85	0.80	0.87	0.90	0.87	0.85	0.91	0.82	0.89	0.86
Pre	0.85	0.85	0.89	0.90	0.88	0.87	0.92	0.84	0.90	0.87
$F_1$ score	0.85	0.84	0.87	0.90	0.87	0.86	0.91	0.83	0.89	0.86
Auc	0.90	0.91	0.96	0.98	0.93	0.92	0.98	0.96	0.97	0.97

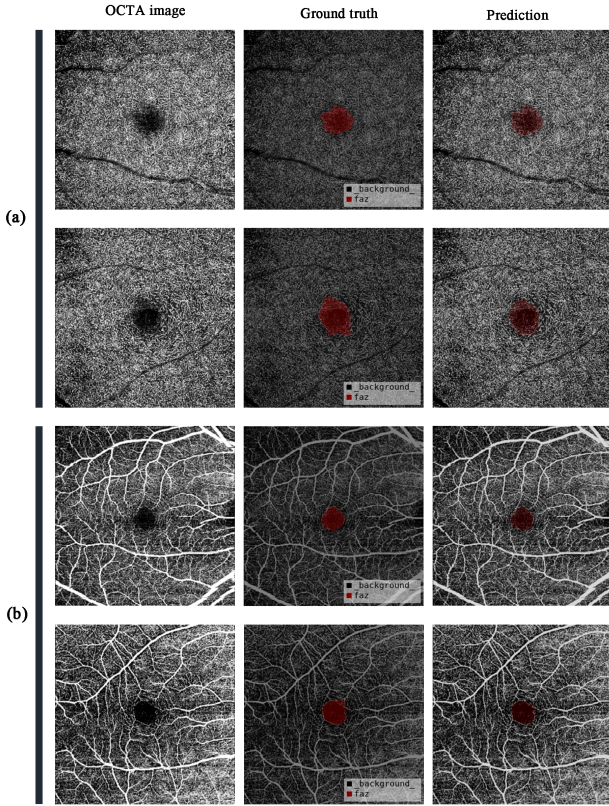


Figure 7. Segmentation results of  $6 \times 6 \text{ mm}^2$  OCTA images against the ground truth. (a) Prediction of dOCTA images; (b) Prediction of sOCTA images.

Table 7. Overall performance of trained FAZ segmentation model on two datasets

Metrics	sOCTA- $3 \times 3$ -1.1k-seg	dOCTA- $6 \times 6$ -1.1k-seg
Dice coefficient	0.95	0.89
Jaccard index	0.91	0.79
Precision	0.96	0.89
Recall	0.95	0.89

alization ability to be extended to all storage format OCTA images by conversion into unified PNG format for processing, assess and classify the images, segment and quantify FAZ and report the results automatically. Compared with existing research [24, 23, 30, 26], our methods achieve outstanding performance, which suggests that this system can

provide a convincing result of OCTA quality assessment as well as FAZ segmentation.

Another major contribution is that we make the first attempt at constructing a public available large-scale dataset containing four sub-datasets, namely sOCTA- $3 \times 3$ -10k, sOCTA- $6 \times 6$ -14k, sOCTA- $3 \times 3$ -1.1k-seg, and dOCTA- $6 \times 6$ -1.1k-seg. To our best knowledge, the dataset is the largest one in this field up to now. We trained each of these five OCTA IQA models: ResNet-101, Inception-V3, Efficientnet-B7, SE-ResNeXt-101, and Swin-Transformer-Large on sOCTA- $3 \times 3$ -10k and sOCTA- $6 \times 6$ -14k dataset and evaluated the performance on the testing set, internal testing set, and external testing set, respectively. For  $3 \times 3 \text{ mm}^2$  sOCTA quality assessment, Swin-Transformer-Large did better than other models and achieved an accuracy of 0.91, a precision of 0.92, and an  $F_1$  score of 0.91. For  $6 \times 6 \text{ mm}^2$  sOCTA quality assessment, SE-ResNeXt-101 did better than other models and achieved an accuracy of 0.90, a precision of 0.90, and an  $F_1$  score of 0.90. In this study, the number of each category per dataset varies greatly. A modified cross-entropy loss function was employed to train the models. The results show that there are no significant differences in prediction performance among the three categories. In view of the importance of FAZ, we trained a U-Net-like architecture based on nnU-Net framework to segment FAZ and quantify the area. The FAZ segmentation models obtained a dice of 0.95 based on sOCTA- $3 \times 3$ -1.1k-seg dataset and a dice of 0.89 based on dOCTA- $6 \times 6$ -1.1k-seg dataset. The different performance of the model on two datasets may be caused by the different features of the OCTA images. The boundary of  $6 \times 6 \text{ mm}^2$  OCTA images is not as clear as  $3 \times 3 \text{ mm}^2$  OCTA images, which makes FAZ area location more difficult. To sum up, the results indicate that deep learning methods are competent for classification and segmentation jobs upon OCTA images and have a broad scope in ophthalmology.

The COIPS we developed made quality assessment and FAZ area quantification very efficient, rendering it practicable for clinical applications. In the future, promising improvements could be achieved by the following aspects: (1) evaluate and verifying COIPS on a new dataset in a clinical setting; (2) inference stage performance speed up; (3) fine-tune the feature extractor to get a higher precision of each category.

## References

- [1] Richard F Spaide, James M Klancnik, and Michael J Cooney, "Retinal vascular layers imaged by fluorescein angiography and optical coherence tomography angiography," *JAMA ophthalmology*, vol. 133, no. 1, pp. 45–50, 2015.
- [2] Richard B Rosen, Jorge S Andrade Romo, Brian D Krawitz, Shelley Mo, Amani A Fawzi, Rachel E Linderman, Joseph Carroll, Alexander Pinhas, and Toco YP Chui, "Earliest evidence of preclinical diabetic retinopathy revealed using optical coherence tomography angiography perfused capillary density," *American journal of ophthalmology*, vol. 203, pp. 103–115, 2019.
- [3] Jost L Laueremann, Nicole Eter, and Florian Alten, "Optical coherence tomography angiography offers new insights into choriocapillaris perfusion," *Ophthalmologica*, vol. 239, no. 2-3, pp. 74–84, 2018.
- [4] Emil AT Say, Sandor Ferenczy, George N Magrath, Wasim A Samara, Chloe TL Khoo, and Carol L Shields, "Image quality and artifacts on optical coherence tomography angiography: comparison of pathologic and paired fellow eyes in 65 patients with unilateral choroidal melanoma treated with plaque radiotherapy," *Retina*, vol. 37, no. 9, pp. 1660–1673, 2017.
- [5] V Manjunath, V Papastavrou, DHW Steel, G Menon, R Taylor, T Peto, and J Talks, "Wide-field imaging and oct vs clinical evaluation of patients referred from diabetic retinopathy screening," *Eye*, vol. 29, no. 3, pp. 416–423, 2015.
- [6] Ian Holmen, Sri Meghana Konda, Jeong W Pak, Barbara A Blodi, Kimberly E Stepien, and Amitha Domalpally, "Assessment of oct angiography image quality in clinical studies," *Investigative Ophthalmology & Visual Science*, vol. 60, no. 9, pp. 3088–3088, 2019.
- [7] Jost B Jonas, Ulrike Schneider, and Gottfried OH Naumann, "Count and density of human retinal photoreceptors," *Graefe's Archive for Clinical and Experimental Ophthalmology*, vol. 230, no. 6, pp. 505–510, 1992.
- [8] Dao-Yi Yu, Stephen J Cringle, and Er-Ning Su, "Intraretinal oxygen distribution in the monkey retina and the response to systemic hyperoxia," *Investigative ophthalmology & visual science*, vol. 46, no. 12, pp. 4728–4733, 2005.
- [9] Chandrakumar Balaratnasingam, Maiko Inoue, Seungjun Ahn, Jesse McCann, Elona Dhrami-Gavazi, Lawrence A Yannuzzi, and K Bailey Freund, "Visual acuity is correlated with the area of the foveal avascular zone in diabetic retinopathy and retinal vein occlusion," *Ophthalmology*, vol. 123, no. 11, pp. 2352–2367, 2016.
- [10] Manuel Casselholmde Salles, Anders Kvanta, Urban Amrén, and David Epstein, "Optical coherence tomography angiography in central retinal vein occlusion: correlation between the foveal avascular zone and visual acuity," *Investigative ophthalmology & visual science*, vol. 57, no. 9, pp. OCT242–OCT246, 2016.
- [11] Khalil Ghasemi Falavarjani and David Sarraf, "Optical coherence tomography angiography of the retina and choroid; current applications and future directions," *Journal of current ophthalmology*, vol. 29, no. 1, pp. 1, 2017.
- [12] Wasim A Samara, Abtin Shahlaee, Murtaza K Adam, M Ali Khan, Allen Chiang, Joseph I Maguire, Jason Hsu, and Allen C Ho, "Quantification of diabetic macular ischemia using optical coherence tomography angiography and its relationship with visual acuity," *Ophthalmology*, vol. 124, no. 2, pp. 235–244, 2017.
- [13] Noriaki Takase, Miho Nozaki, Aki Kato, Hironori Ozeki, Munenori Yoshida, and Yuichiro Ogura, "Enlargement of foveal avascular zone in diabetic eyes evaluated by en face optical coherence tomography angiography," *Retina*, vol. 35, no. 11, pp. 2377–2383, 2015.
- [14] Hirokazu Ishii, Takuhei Shoji, Yuji Yoshikawa, Junji Kanno, Hisashi Ibuki, and Kei Shinoda, "Automated measurement of the foveal avascular zone in swept-source optical coherence tomography angiography images," *Translational vision science & technology*, vol. 8, no. 3, pp. 28–28, 2019.
- [15] Aidi Lin, Danqi Fang, Cuilian Li, Carol Y Cheung, and Haoyu Chen, "Reliability of foveal avascular zone metrics automatically measured by cirrus optical coherence tomography angiography in healthy subjects," *International ophthalmology*, vol. 40, no. 3, pp. 763–773, 2020.
- [16] George N Magrath, Emil Anthony T Say, Kareem Sioufi, Sandor Ferenczy, Wasim A Samara, and Carol L Shields, "Variability in foveal avascular zone and capillary density using optical coherence tomography angiography machines in healthy eyes," *Retina*, vol. 37, no. 11, pp. 2102–2111, 2017.
- [17] Yong Pi, Zhen Zhao, Yongzhao Xiang, Yuhao Li, Huawei Cai, and Zhang Yi, "Automated diagnosis of



- bone metastasis based on multi-view bone scans using attention-augmented deep neural networks,” *Medical Image Analysis*, vol. 65, pp. 101784, 2020.
- [18] Rajeev Ranjan, Vishal M Patel, and Rama Chellappa, “Hyperface: A deep multi-task learning framework for face detection, landmark localization, pose estimation, and gender recognition,” *IEEE transactions on pattern analysis and machine intelligence*, vol. 41, no. 1, pp. 121–135, 2017.
- [19] Jingxiang Yang, Yong-Qiang Zhao, and Jonathan Cheung-Wai Chan, “Learning and transferring deep joint spectral–spatial features for hyperspectral classification,” *IEEE Transactions on Geoscience and Remote Sensing*, vol. 55, no. 8, pp. 4729–4742, 2017.
- [20] Yiqing Shen and Jing Ke, “Sampling based tumor recognition in whole-slide histology image with deep learning approaches,” *IEEE/ACM Transactions on Computational Biology and Bioinformatics*, 2021.
- [21] Yiqing Shen and Jing Ke, “Representative region based active learning for histological classification of colorectal cancer,” in *2021 IEEE 18th International Symposium on Biomedical Imaging (ISBI)*. IEEE, 2021, pp. 1730–1733.
- [22] Minhaj Alam, David Le, Jennifer I Lim, Robison VP Chan, and Xincheng Yao, “Supervised machine learning based multi-task artificial intelligence classification of retinopathies,” *Journal of clinical medicine*, vol. 8, no. 6, pp. 872, 2019.
- [23] JL Lauermaann, M Treder, M Alnawaiseh, CR Clemens, N Eter, and F Alten, “Automated oct angiography image quality assessment using a deep learning algorithm,” *Graefe’s Archive for Clinical and Experimental Ophthalmology*, vol. 257, no. 8, pp. 1641–1648, 2019.
- [24] Ylenia Giarratano, Eleonora Bianchi, Calum Gray, Andrew Morris, Tom MacGillivray, Baljean Dhillon, and Miguel O Bernabeu, “Automated segmentation of optical coherence tomography angiography images: benchmark data and clinically relevant metrics,” *Translational vision science & technology*, vol. 9, no. 13, pp. 5–5, 2020.
- [25] Menglin Guo, Mei Zhao, Allen MY Cheong, Federico Corvi, Xin Chen, Siping Chen, Yongjin Zhou, and Andrew KC Lam, “Can deep learning improve the automatic segmentation of deep foveal avascular zone in optical coherence tomography angiography?,” *Biomedical Signal Processing and Control*, vol. 66, pp. 102456, 2021.
- [26] Reza Mirshahi, Pasha Anvari, Hamid Riazi-Esfahani, Mahsa Sardarinia, Masood Naseripour, and Khalil Ghasemi Falavarjani, “Foveal avascular zone segmentation in optical coherence tomography angiography images using a deep learning approach,” *Scientific reports*, vol. 11, no. 1, pp. 1–8, 2021.
- [27] Yukun Guo, Acner Camino, Jie Wang, David Huang, Thomas S Hwang, and Yali Jia, “Mednet, a neural network for automated detection of avascular area in oct angiography,” *Biomedical optics express*, vol. 9, no. 11, pp. 5147–5158, 2018.
- [28] Xiayu Xu, Cheng Chen, Wenxiang Ding, Peiwei Yang, Huiqin Lu, Feng Xu, and Jianqin Lei, “Automated quantification of superficial retinal capillaries and large vessels for diabetic retinopathy on optical coherence tomographic angiography,” *Journal of biophotonics*, vol. 12, no. 11, pp. e201900103, 2019.
- [29] Yukun Guo, Tristan T Hormel, Honglian Xiong, Bingjie Wang, Acner Camino, Jie Wang, David Huang, Thomas S Hwang, and Yali Jia, “Development and validation of a deep learning algorithm for distinguishing the nonperfusion area from signal reduction artifacts on oct angiography,” *Biomedical optics express*, vol. 10, no. 7, pp. 3257–3268, 2019.
- [30] Aidi Lin, Danqi Fang, Cuilian Li, Carol Y Cheung, and Haoyu Chen, “Improved automated foveal avascular zone measurement in cirrus optical coherence tomography angiography using the level sets macro,” *Translational vision science & technology*, vol. 9, no. 12, pp. 20–20, 2020.
- [31] Dongxu Gao, Numan Celik, Xiyin Wu, Bryan M Williams, Amira Stylianides, and Yalin Zheng, “A novel deep learning based octa de-stripping method,” in *Annual Conference on Medical Image Understanding and Analysis*. Springer, 2019, pp. 189–197.
- [32] Ian C Holmen, Sri Meghana Konda, Jeong W Pak, Kyle W McDaniel, Barbara Blodi, Kimberly E Stepien, and Amitha Domalpally, “Prevalence and severity of artifacts in optical coherence tomographic angiograms,” *JAMA ophthalmology*, vol. 138, no. 2, pp. 119–126, 2020.
- [33] SanaUllah Khan, Naveed Islam, Zahoor Jan, Ikram Ud Din, and Joel JP C Rodrigues, “A novel deep learning based framework for the detection and classification of breast cancer using transfer learning,” *Pattern Recognition Letters*, vol. 125, pp. 1–6, 2019.
- [34] Zar Nawab Khan Swati, Qinghua Zhao, Muhammad Kabir, Farman Ali, Zakir Ali, Saeed Ahmed, and Jian-

- feng Lu, “Brain tumor classification for mr images using transfer learning and fine-tuning,” *Computerized Medical Imaging and Graphics*, vol. 75, pp. 34–46, 2019.
- [35] Fuzhen Zhuang, Zhiyuan Qi, Keyu Duan, Dongbo Xi, Yongchun Zhu, Hengshu Zhu, Hui Xiong, and Qing He, “A comprehensive survey on transfer learning,” *Proceedings of the IEEE*, vol. 109, no. 1, pp. 43–76, 2020.
- [36] Kaiming He, Xiangyu Zhang, Shaoqing Ren, and Jian Sun, “Deep residual learning for image recognition,” in *Proceedings of the IEEE conference on computer vision and pattern recognition*, 2016, pp. 770–778.
- [37] Christian Szegedy, Vincent Vanhoucke, Sergey Ioffe, Jon Shlens, and Zbigniew Wojna, “Rethinking the inception architecture for computer vision,” in *Proceedings of the IEEE conference on computer vision and pattern recognition*, 2016, pp. 2818–2826.
- [38] Mingxing Tan and Quoc Le, “Efficientnet: Rethinking model scaling for convolutional neural networks,” in *International Conference on Machine Learning*. PMLR, 2019, pp. 6105–6114.
- [39] Jie Hu, Li Shen, and Gang Sun, “Squeeze-and-excitation networks,” in *Proceedings of the IEEE conference on computer vision and pattern recognition*, 2018, pp. 7132–7141.
- [40] Saining Xie, Ross Girshick, Piotr Dollár, Zhuowen Tu, and Kaiming He, “Aggregated residual transformations for deep neural networks,” in *Proceedings of the IEEE conference on computer vision and pattern recognition*, 2017, pp. 1492–1500.
- [41] Ze Liu, Yutong Lin, Yue Cao, Han Hu, Yixuan Wei, Zheng Zhang, Stephen Lin, and Baining Guo, “Swin transformer: Hierarchical vision transformer using shifted windows,” *arXiv preprint arXiv:2103.14030*, 2021.
- [42] Pieter-Tjerk De Boer, Dirk P Kroese, Shie Mannor, and Reuven Y Rubinfeld, “A tutorial on the cross-entropy method,” *Annals of operations research*, vol. 134, no. 1, pp. 19–67, 2005.
- [43] Bo Zhou, Zachary Augenfeld, Julius Chapiro, S. Kevin Zhou, Chi Liu, and James S. Duncan, “Anatomy-guided multimodal registration by learning segmentation without ground truth: Application to intraprocedural cbct/mr liver segmentation and registration,” *Medical Image Analysis*, vol. 71, pp. 102041, 2021.
- [44] Thorsten Falk, Dominic Mai, Robert Bensch, Özgün Çiçek, Ahmed Abdulkadir, Yassine Marrakchi, Anton Böhm, Jan Deubner, Zoe Jäckel, Katharina Seiwald, et al., “U-net: deep learning for cell counting, detection, and morphometry,” *Nature methods*, vol. 16, no. 1, pp. 67–70, 2019.
- [45] Olaf Ronneberger, Philipp Fischer, and Thomas Brox, “U-net: Convolutional networks for biomedical image segmentation,” in *International Conference on Medical image computing and computer-assisted intervention*. Springer, 2015, pp. 234–241.
- [46] Fabian Isensee, Paul F Jaeger, Simon AA Kohl, Jens Petersen, and Klaus H Maier-Hein, “nnu-net: a self-configuring method for deep learning-based biomedical image segmentation,” *Nature methods*, vol. 18, no. 2, pp. 203–211, 2021.
- [47] Kelei He, Chunfeng Lian, Bing Zhang, Xin Zhang, Xiaohuan Cao, Dong Nie, Yang Gao, Junfeng Zhang, and Dinggang Shen, “Hf-unet: Learning hierarchically inter-task relevance in multi-task u-net for accurate prostate segmentation in ct images,” *IEEE Transactions on Medical Imaging*, 2021.
- [48] Adnan Saood and Iyad Hatem, “Covid-19 lung ct image segmentation using deep learning methods: U-net versus segnet,” *BMC Medical Imaging*, vol. 21, no. 1, pp. 1–10, 2021.
- [49] Zongwei Zhou, Md Mahfuzur Rahman Siddiquee, Nima Tajbakhsh, and Jianming Liang, “Unet++: Redesigning skip connections to exploit multiscale features in image segmentation,” *IEEE transactions on medical imaging*, vol. 39, no. 6, pp. 1856–1867, 2019.
- [50] Jia Deng, Wei Dong, Richard Socher, Li-Jia Li, Kai Li, and Li Fei-Fei, “Imagenet: A large-scale hierarchical image database,” in *2009 IEEE conference on computer vision and pattern recognition*. Ieee, 2009, pp. 248–255.
- [51] Diederik P Kingma and Jimmy Ba, “Adam: A method for stochastic optimization,” *arXiv preprint arXiv:1412.6980*, 2014.
- [52] Ilya Loshchilov and Frank Hutter, “Fixing weight decay regularization in adam,” 2018.
- [53] Ilya Loshchilov and Frank Hutter, “Sgdr: Stochastic gradient descent with warm restarts,” *arXiv preprint arXiv:1608.03983*, 2016.
- [54] Léon Bottou, *Stochastic Gradient Descent Tricks*, pp. 421–436, Springer Berlin Heidelberg, Berlin, Heidelberg, 2012.

- [55] Liang-Chieh Chen, George Papandreou, Iasonas Kokkinos, Kevin Murphy, and Alan L Yuille, “Deeplab: Semantic image segmentation with deep convolutional nets, atrous convolution, and fully connected crfs,” *IEEE transactions on pattern analysis and machine intelligence*, vol. 40, no. 4, pp. 834–848, 2017.